Transient Stability of Meshed HVDC Offshore Wind Network within New York State Power Grid

Lokesh Saravana
ECE Department
Clarkson University
Potsdam, USA
saraval@clarkson.edu

Xuan Phuong Nguyen
ECE Department
Clarkson University
Potsdam, USA
nguyenx@clarkson.edu

Shuvangkar Chandra Das
ECE Department
Clarkson University
Potsdam, USA
dassc@clarkson.edu

Jianhua Zhang
ECE Department
Clarkson University
Potsdam, USA
jzhang@clarkson.edu

Tuyen V. Vu
ECE Department
Clarkson University
Potsdam, USA
tvu@clarkson.edu

Thomas Ortmeyer
ECE Department
Clarkson University
Potsdam, USA
tortmeye@clarkson.edu

Victor D. Paduani
AGILe
New York Power Authority
Albany, NY, USA
Victor.DaldeganPaduani@nypa.gov

***Abstract*—This paper investigates transient and voltage stability of a meshed HVDC offshore network integrated to the New York State grid on a real-time OPAL-RT-RTDS co-simulation platform linked by a Transmission Line Modeling (TLM) fiber-optic interface. Each offshore grid-forming (GFM) converter employs P–f/Q–V droop with a positive-sequence dq PI voltage loop, augmented by a virtual-resistance fault-ride-through (FRT) scheme. We subject the system to representative disturbances—converter-terminal faults, AC-mesh line faults, point-of-interconnection (POI) contingencies with realistic clearing times, and a large generator trip—and evaluate active/reactive power sharing, frequency excursions, POI voltage recovery, settling time, and critical clearing time (CCT). Results show successful ride-through of POI faults and generator trips, clear trend of transient magnitude with longer clearing times, and that lower dispatch increases critical clearing time while local VAR support enables longer CCT. The study provides a system-scale EMT validation of virtual-resistance FRT in AC-meshed topologies and maps stability versus SCR and dispatch, offering practical guidance for shunt device scheduling tuning and VAR planning in converter-dominated networks.**

***Index Terms*—meshed HVDC offshore grid, system-scale EMT validation, fault ride-through, voltage stability, transient stability**

I. Introduction

HVDC interfacing of offshore wind with meshed AC collection networks offers scalability and redundancy, while grid-forming converters provide voltage-forming capability and inertia-like support in converter-dominated grids. In converter-dominated systems, stability depends on the interplay between GFM control, FRT behavior, short-circuit strength, and network impedance [1], [2]. This work examines transient and voltage stability of a meshed HVDC offshore network, emphasizing realistic clearing times, and operating-point sensitivity.

In recent literature on AC-side meshed HVDC networks, Rodríguez-Amenedo et al [3] analyzes an AC-side meshed HVDC network with two Voltage Source Converters (VSC)-HVDC links sharing power via offshore voltage regulation. The study shows that low-resistance export cables yield a high voltage-to-power gain, which makes power sharing difficult with sometimes under-damped behavior unless reactors, filters, or supervisory coordination are added. To address this, [4] introduces coordinated schemes in which a grid-forming VSC/Modular Multilevel Converter (MMC) sets the AC reference and a diode-rectifier (DR) HVDC link passively balances active power, improving damping and reducing sensitivity to cable parameters. In [5], Li et al. extend the idea by coordinating DR-HVDC with an MMC-HVDC so the MMC provides energization, voltage support, and dynamic response, and assumes transfer during outages while the DR carries most steady-state power. Similarly, Liu et al. [6] investigates a meshed AC/DC distribution architecture utilizing active power filters and coordinated control to optimize power quality and minimize losses in systems with high levels of distributed photovoltaic sources. For fault ride-through, [7] adopts the virtual-resistance method, which limits current while preserving the voltage-forming role, and has been verified on programmable three-level Active-Neutral-Point Clamped (ANPC) GFMs. Differing from these single-bus (hub-and-spoke) studies, we evaluate an AC-side meshed HVDC network and study system-scale stability metrics—frequency deviation, voltage overshoot, settling time, and CCT. To achieve this, we conduct *transient* and *voltage* stability studies on a system-scale EMT model of a reduced NYS power grid integrated with the AC-side meshed HVDC offshore wind network:

- **System-scale assessment of GFM + virtual-resistance FRT:** We implement a virtual resistance–FRT and quantify its system-scale effects on fault-current limiting, preservation of the voltage-forming reference, and post-fault damping/settling under AC faults.
- **Transient and voltage stability:** We quantify frequency excursions, voltage overshoot, settling times, and CCT across a range of AC fault scenarios with clearing times

This work was supported by the New York State Energy Research and Development Authority (NYSERDA) under Project Award #200833, "De-risk Meshed-ready HVDC for Offshore Wind with Realtime EMT Modeling & Studies." The authors also gratefully acknowledge the collaboration and support provided by AGILe, New York Power Authority, and INS Engineering.

979-8-3315-8138-1

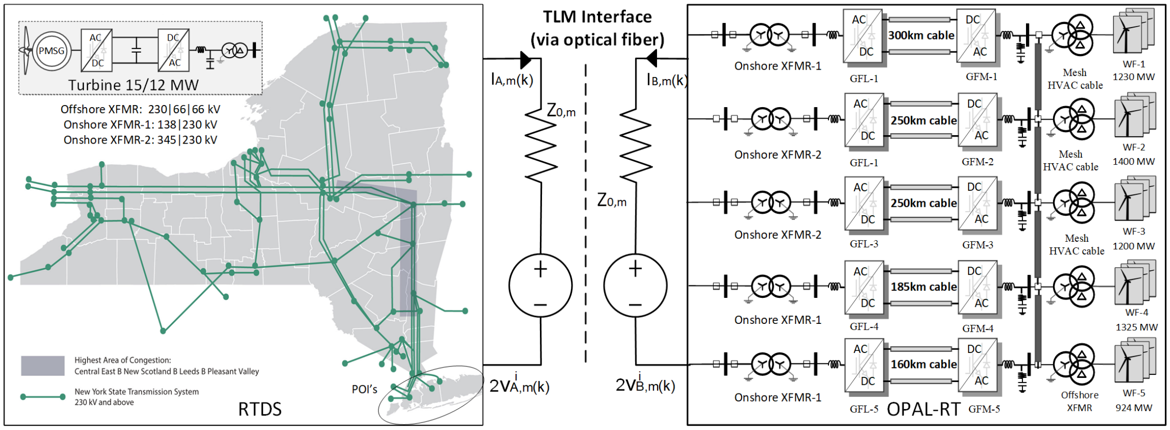

Fig. 1. Top-level diagram of meshed HVDC model with NYS grid

selected to reflect practical protection envelopes.

- **Operating-point sensitivity maps:** We chart stability versus SCR, wind dispatch level, and offshore cable impedances, identifying transitions between well-damped, acceptable, and underdamped/unstable regimes for converter-dominated meshes.

II. Meshed offshore system and fault-ride through logic

A. Large-scale EMT Model of Meshed HVDC and NYS grid

The study considers a meshed HVDC offshore wind network that meshes five offshore wind farms (OWFs) on the offshore substation side through HVAC cables and interconnects to a NYS grid via individual HVDC onshore substation facilities, shown in Fig.1. Each OWF is modeled as an aggregated (15 & 12 MW) wind-turbine block that preserves aerodynamic and drive-train dynamics sufficient for fault and post-fault power recovery [8]. Each OWF is collected on medium-voltage AC collecter system, stepped to 230kV, and connected to the offshore AC meshed cables. Offshore GFM converters operate as rectifiers and feed the HVDC links, while onshore grid-following (GFL) converters act as inverters at the points of interconnection, converting DC back to AC. The meshed HVDC offshore wind network provides multiple transfer paths between OWFs and the onshore grid, enabling power sharing during disturbances and planned outages. The NYS grid is modeled using a reduced-order 500-bus summer peak case. In this work, a meshed HVDC offshore wind network is modeled in OPAL-RT and co-simulated with the New York State Power System (NYSPS) in RTDS via a TLM fiber-optic interface. As shown, the network is partitioned at multiple TLM interfaces indexed by $m = 1, .., 5$. Each side of interface m is terminated by the characteristic impedance $Z_{0,m}$ and exchanges incident voltages $2V^i_{A,m}$, $2V^i_{B,m}$ over the fiber link, while measuring port currents $I_{A,m}$, $I_{B,m}$. With a two–step delay (time step considered is 50 μs), the coupling is as follows:

$$2V^i_{A,m}(k) = V_{B,m}(k-1) + I_{B,m}(k-1)\, Z_{0,m} \quad (1)$$

$$2V^i_{B,m}(k) = V_{A,m}(k-1) + I_{A,m}(k-1)\, Z_{0,m} \quad (2)$$

which lets each simulator exchanges data independently. The characteristic impedance is chosen from the line parameters as

$$Z_{0,m} = \frac{L_m}{T} \quad \text{or} \quad Z_{0,m} = \frac{T}{C_m},$$

where T is the propagation delay across the interface, and L_m and C_m are the inductance and capacitance associated with the line seen at interface m [9] [10].

B. MGCC Controller and FRT Logic

Under normal conditions, each offshore GFM converter regulates voltage and frequency using droop control cascaded with a positive-sequence dq-frame PI voltage regulator. Active–power–frequency (P–f) droop updates the frequency/phase, while reactive–power–voltage (Q–V) droop sets the voltage magnitude reference that feeds the PI controller voltage loop, and the q-axis reference is held at zero for alignment. Power setpoints $(P_{\text{ref}}, Q_{\text{ref}})$ are provided by the Meshed Grid Co-ordinated controller (MGCC). The MGCC is a centralized supervisory controller for multiple OWF platforms connected via an AC mesh and HVDC links. It issues $(P_{\text{ref}}, Q_{\text{ref}})$ setpoints to offshore GFM converters, manages topology/breaker actions and contingency routing, and schedules local VAR resources to maintain POI voltages using plant measurements. FRT is executed locally in each offshore GFM converter, which preserves stability during short-duration faults and enables scalable "meshed-ready" expansion with minimal retrofit.

FRT detection and action: During a fault, the controller continuously monitors the inductor-current magnitude computed from (i) the peak of the instantaneous phase currents $I^p = \max\{I^s_a, I^s_b, I^s_c\}$ and (ii) the positive-sequence current magnitude $\|I^{s+}_{dq}\| = \sqrt{(I^{s+}_d)^2 + (I^{s+}_q)^2}$. The negative-sequence components I^{s-}_{dq} are observed for unbalance diagnosis but are not used to arm the FRT trigger [7]. When I^p exceeds the threshold for longer than the arming delay ($t > t_{set}$), the logic: (1) sets the fault-detection flag $FD \in \{0,1\}$; (2) freezes the voltage-loop integrator and suspends droop/frequency updates to prevent wind-up and drift; and (3)

979-8-3315-8138-1

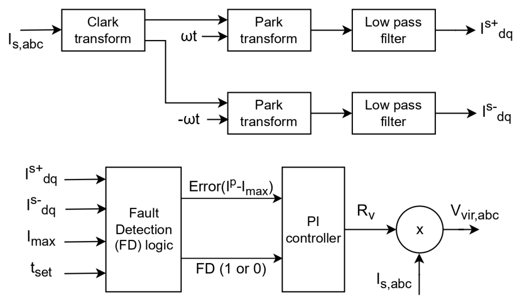

Fig. 2. Block diagram of FRT logic.

activates an auxiliary PI ($K_p = 2, K_i = 100$) that acts on the current-limit error to synthesize a virtual resistance R_v [7]. The resulting virtual voltage

$$\boldsymbol{v}_{\text{vir},abc} = R_v\, \boldsymbol{i}_{s,abc} \tag{3}$$

is subtracted from the modulator reference just before PWM, temporarily increasing the converter's apparent output impedance. Here, $\boldsymbol{i}_{s,abc}$ is the measured instantaneous phase-current vector at the converter AC terminals. This limits fault current while maintaining voltage-forming capability and supports a smooth post-fault recovery to nominal [7].

III. Simulation Results

Based on the developed large-scale EMT model of the NYS grid and meshed HVDC offshore wind network, we conduct intensive analysis, including transient stability, voltage stability, and sensitivity analysis, across wide-range predefined stability scenarios. The validation results and discussion are presented in this section.

A. Transient Stability

Case 1: GFM Converter 2, 3P-G Fault (0.1 s, 6 cycles) A balanced three-phase-to-ground fault is applied at GFM Converter 2 at $t = 31$ s and cleared after 0.1 s. As shown in Fig. 3, the active and reactive power responses in subfigures (a) and (b) exhibit brief dips when the fault happens at $t = 31$ s, but surge immediately after fault clearance, and they quickly settle back to their pre-fault levels. The frequency response in Fig. 3 (c) remains well regulated with a maximum deviation below 0.2 Hz that damps out quickly. The POI voltage response in Fig. 3 (d) displays a brief disturbance and remains within acceptable operational limits throughout the event.

Case 2: GFM Converter 5, SLG Fault (0.1 s, 6 cycles) A single-line-to-ground fault is applied at GFM Converter 5 at $t = 27.5$ s and cleared after 0.1 s. As shown in Fig. 4, the active and reactive power responses and the POI voltage response in Fig. 4 (a), (b) and (d) show sharp dips and spikes immediately following the fault, with GFM5 exhibiting the largest deviation; however, all converters resettle quickly once the fault is cleared and remains within operational limits throughout the event. The frequency response in Fig. 4 (c) exhibits a minor oscillation of less than 0.2 Hz that damps out within a few seconds.

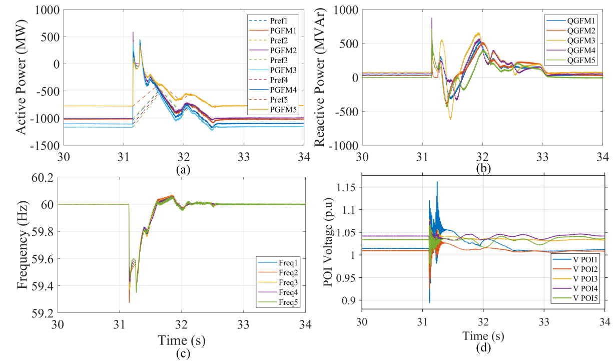

Fig. 3. Results for GFM2, 3P-G, 6 cycles (0.1s)

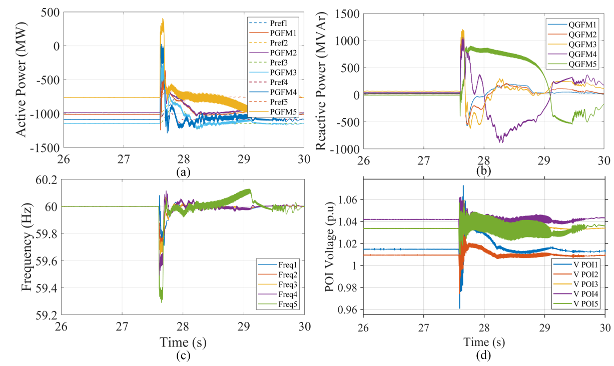

Fig. 4. Results for GFM5, SLG, 6 cycles (0.1s)

Case 3: Mesh Cable Between GFM4 and GFM5, 3P-G Fault (0.067 s, 4 cycles) A contingency is first introduced at GFM5 at $t = 2$ s, causing power from WF5 to be rerouted through the mesh cable to GFM4. Subsequently, a balanced 3P–G fault is applied on the mesh cable connecting GFM4 and GFM5 at $t = 13.5$ s. The breaker opens at $t = 13.517$ s, the fault is cleared at $t = 13.567$ s, and the breaker recloses at $t = 13.583$ s. The active responses in Fig. 5(a) exhibit sharp surges immediately after fault application and breaker operation. These transients correspond to rapid power redistribution across converters. When the breaker opens, the faulted path is isolated, creating a temporary power imbalance. After reclosing time, the power flows gradually settle to their pre-fault steady-state values. The frequency response in Fig. 5(b) shows small oscillations within ± 0.2 Hz that damp quickly, indicating effective frequency support by the grid-forming converters. The meshed active power exchange and onshore delivery in Fig. 5(c) experience noticeable disturbances when the breaker isolates the faulted section, followed by rapid rebalancing once the fault is cleared. Finally, the POI voltage in Fig. 5(d) show brief deviations that remain within operational limits.

Case 4: WF-2 POI, 3P-G (0.05 s, 3 cycles) A balanced three-phase-to-ground fault is applied at the WF-2 POI which is identified as a weak POI at $t = 8$ s and cleared after 0.05 s. As shown in Fig. 6, the active power response in subfigure (a) shows a short-duration dip and surge before quickly re-tracking its reference value. The frequency trace in Fig. 6(b) exhibits small oscillations that damp rapidly. The

979-8-3315-8138-1

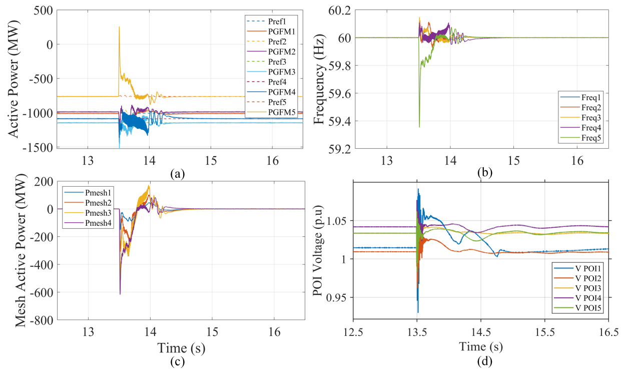

Fig. 5. Results for Mesh cable between GFM4 and 5, 3P-G, 4 cycles (0.067s)

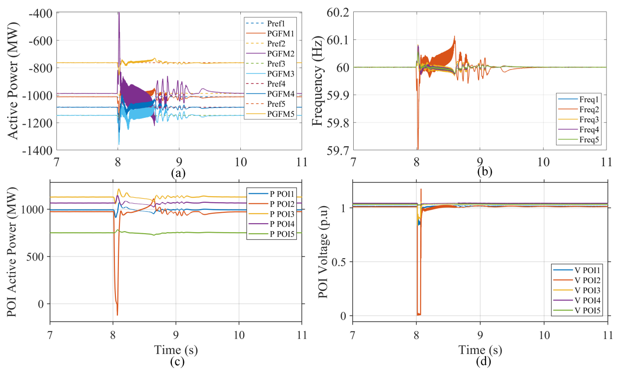

Fig. 6. Results for GFM-2 POI, 3P-G, 0.05 s

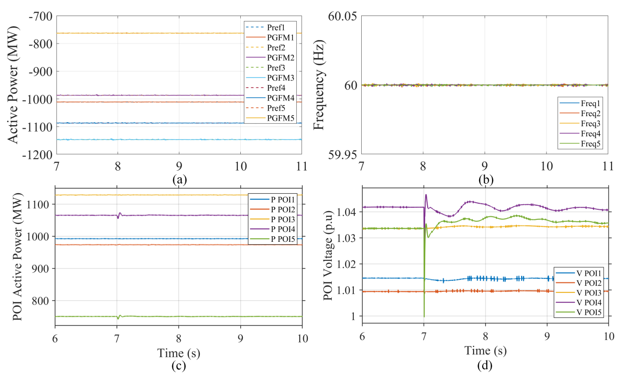

Fig. 7. Results for Largest generators trip

POI active power and the POI voltage in Fig. 6(c) and (d) remains within expected operational limits with a brief sag and smooth recovery to steady-state.

Case 5: Onshore Largest generator trip (≈ 3600 MW equivalent) A sudden generator trip of approximately 3×1200 MW is applied at $t = 7$ s. As shown in Fig. 7, the active power response in subfigure (a) exhibits smooth rebalancing with rapid tracking back to its reference. The frequency trace in Fig. 7(b) shows a small, well-damped excursion. The POI voltage in Fig. 7(c) stays within acceptable limits with only a brief deviation, and the POI active power in Fig. 7(d) displays a minor step change followed by prompt return to nominal.

B. Voltage Stability

Case 6: WF-2 POI, 3P–G (0.1 s, 6 cycles), 60% dispatch, no shunt device A balanced 3P-G fault is applied at $t = 8.7$ s and cleared after 0.1 s (6 cycles). As shown in Fig. 8, most system variables remain stable following fault clearance. The GFM active power responses of five WFs in Fig. 8(a) shows brief dips and surges before returning toward their references, frequency deviations in Fig. 8(b) are small and well damped. Additionally, the offshore WF-2 instantaneous converter terminal voltage in Fig. 8(d) stays in the range of 0.9–1.1 p.u. band and 7.87% overshoot after clearing within 3.86 s from fault inception.

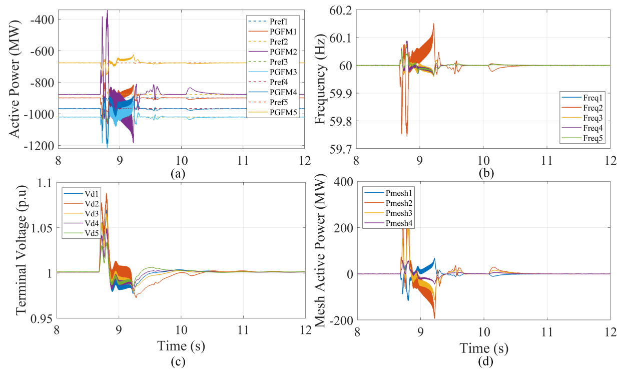

Fig. 8. Results for WF-2, 3P-G (0.1 s), 60% dispatch, no shunt device

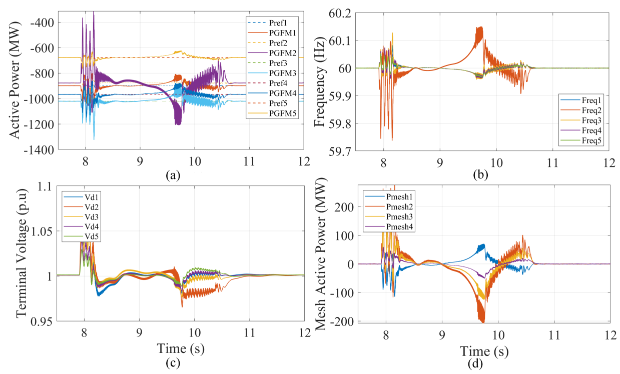

Fig. 9. Results for WF-2 POI, 3P-G, 60% dispatch, 0.167 s, shunt capacitor added

Case 7: WF-2 POI, 3P–G (0.167 s, 10 cycles), 60% dispatch, shunt capacitor on — As shown in Fig. 9, with the fault applied at $t = 8$ s, panels Fig. 9(a)–(b), (d) remain stable GFM active power exhibits a brief dip/surge, then retracks their references; frequency excursions are small and well damped, and meshed power settles promptly. The notable change is in Fig. 9(c): with the shunt capacitor in service, the terminal voltage remains stable and returns to its acceptable band, in clear contrast to Case 6, where the terminal voltage failed to resettle and dropped outside the 0.9–1.1 p.u. range, and showing improvement in terms of critical clearing time (from 6 cycles to 10 cycles). This confirms that added capacitive VAR support stabilizes the post-fault voltage response under the longer clearing time.

C. Sensitivity Analysis

Case 8: WF-2 POI, 3P–G (0.083 s, 5 cycles), 85% dispatch, weak grid (SCR=1.2) Figure 10 illustrates loss of voltage stability under high wind dispatch and low SCR con-

979-8-3315-8138-1

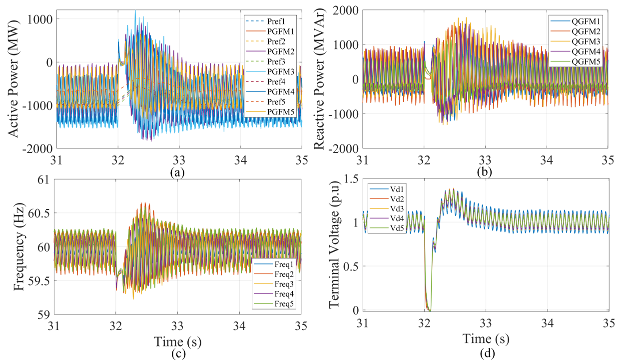

Fig. 10. Results for Case wind dispatch 85%, weak grid, 3P-G 5 cycles fault at WF-2

ditions. The active and reactive power traces in Fig. 10(a)–(b) show large post-fault swings that fail to re-track their reference values and remain oscillatory. The frequency response in Fig. 10(c) shows a sustained low-frequency oscillation rather than the short, well-damped deviation observed in lower-dispatch cases. The voltage in Fig. 10(d) drops deeply during the fault, overshoot beyond the acceptable operating band, and fails to resettle within 0.9–1.1 p.u. This instability arises from the combined stress of high active power export (85% dispatch) and weak grid strength (SCR = 1.2), which amplifies converter–grid interactions and reduces effective voltage stiffness. Consequently, both power and voltage exhibit persistent oscillations, confirming a loss of dynamic voltage stability.

Case 9: WF-2 POI, 3P–G (0.083 s, 5 cycles), 85% dispatch, strong grid (SCR=10) The SCR was varied by adjusting the magnitude of the onshore-grid Thevenin equivalent impedance at the POI to achieve SCR levels of 1.2 and 10, while maintaining a constant X/R ratio. This was done without altering the network topology or dispatch. Figure 11 demonstrates that restoring short-circuit strength recovers stability under the same high-export condition. Compared to Case 8, the active and reactive power responses in Fig. 11(a)–(b) exhibit smaller transients at fault clearance and rapidly return to their setpoints. The frequency in Fig. 11(c) remains regulated around 60 Hz with only a brief, well-damped deviation. The voltage in Fig. 11(d) exhibits a shallower dip and a limited overshoot, resettling within 0.9–1.1 p.u. in less than 2.5 s. Overall, the increased SCR offsets the dynamic stress associated with high dispatch, restoring sufficient voltage margin and stable post-fault recovery. Stronger grid conditions improve synchronization, enhance damping, where the cumulative duration of the instantaneous phase-to-ground overvoltage was limited to less than 0.1 s, remaining well within the transient overvoltage ride-through requirement of IEEE 2800-2022 and IEC 60071 transient limits.

IV. Conclusion

We demonstrated a real-time OPAL-RT–RTDS co-simulation of a large-scale NYS power grid integrated with 6GW meshed HVDC offshore network with GFM converters and virtual-resistance FRT, showing robust ride-through

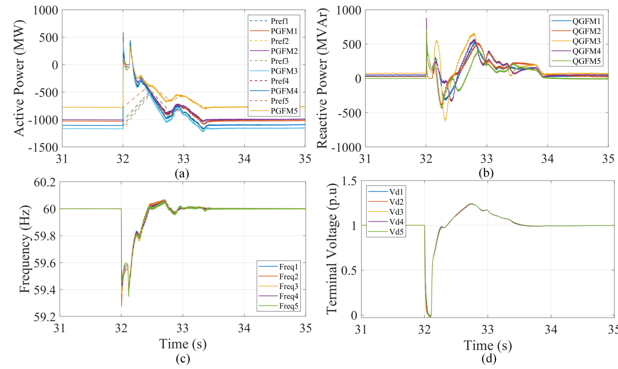

Fig. 11. Results for Case wind dispatch 85%, strong grid, 3P-G 5 cycles fault at WF-2

across converter, AC-mesh, and POI faults and a large generator trip. The weakest point (85% dispatch, SCR = 1.2) exhibited post-fault oscillations and failed to re-enter the 0.90–1.10 p.u. band, highlighting sensitivity to short-circuit strength at high export. Raising SCR to 10 or adding shunt VAR support restored damping and margin, confirming that virtual-resistance FRT preserves voltage-forming while stability depends jointly on controller settings, grid strength, and local reactive support.

References

[1] "Ieee standard for interconnection and interoperability of inverter-based resources (ibrs) interconnecting with associated transmission electric power systems," *IEEE Std 2800-2022*, pp. 1–180, 2022.

[2] NERC, "Reliability guideline: Integrating inverter-based resources into low short circuit strength systems," tech. rep., North American Electric Reliability Corporation, Atlanta, GA, Dec. 2017.

[3] J. L. Rodríguez-Amenedo, S. Arnaltes-Gómez, M. Aragüés-Peñalba, and O. Gomis-Bellmunt, "Control of the parallel operation of vsc-hvdc links connected to an offshore wind farm," *IEEE Transactions on Power Delivery*, vol. 34, no. 1, pp. 32–41, 2019.

[4] A. Nami, J. L. Rodriguez-Amenedo, S. Arnaltes, M. Cardiel-Álvarez, and R. A. Baraciarte, "Control of the parallel operation of dr-hvdc and vsc-hvdc for offshore wind power transmission," *IEEE Transactions on Power Delivery*, vol. 37, no. 3, pp. 1682–1691, 2022.

[5] R. Li, L. Yu, L. Xu, and G. P. Adam, "Coordinated control of parallel dr-hvdc and mmc-hvdc systems for offshore wind energy transmission," *IEEE Journal of Emerging and Selected Topics in Power Electronics*, vol. 8, no. 3, pp. 2572–2582, 2020.

[6] C. Liu, M. Zhang, X. Yang, S. Ji, L. Yang, R. Zhu, and X. Li, "System architecture and coordinated control strategy of meshed ac/dc distribution grid based on active power filter," in *Eighth International Conference on Energy System, Electricity, and Power (ESEP 2023)*, vol. 13159, pp. 2692–2697, SPIE, 2024.

[7] M. S. Hossain, S. C. Das, P. Kritprajun, A. Banaie, T. Barik, D. Ramasubramanian, A. Haddadi, E. Farantatos, and U. Muenz, "Hardware implementation of virtual resistance based frt logic in programmable 3-level anpc inverters," in *2025 IEEE Applied Power Electronics Conference and Exposition (APEC)*, pp. 1184–1189, 2025.

[8] T.-T. Nguyen, T. Vu, T. Ortmeyer, G. Stefopoulos, G. Pedrick, and J. MacDowell, "Real-time transient simulation and studies of offshore wind turbines," *IEEE Transactions on Sustainable Energy*, vol. 14, no. 3, pp. 1474–1487, 2023.

[9] L. Barbierato, E. Pons, and E. e. a. Bompard, "Exploring stability and accuracy limits of distributed real-time power system simulations via system-of-systems cosimulation," in *IEEE Systems Journal*, 2023.

[10] L. Saravana, J. Zhang, T. Ortmeyer, T. V. Vu, and V. D. Paduani, "Irig-b synchronized emt-emt co-simulation framework for opal-rt/rtds integration," in *2025 57th North American Power Symposium (NAPS)*, pp. 1–6, 2025.

979-8-3315-8138-1